Mechanism of Hierarchical Porosity Development in Hexagonal Boron Nitride Nanocrystalline Microstructures for Biomedical and Industrial Applications

Jose Humberto Ramirez Leyva,[†,‡,§] Gerardo Vitale,[†] Afif Hethnawi,[†] Azfar Hassan,[†]
Maria Josefina Perez-Zurita,[†] Guillermo U. Ruiz-Esparza,[‡,§] and Nashaat N. Nassar*,[†]

[†]Department of Chemical and Petroleum Engineering, University of Calgary, 2500 University Drive NW, Calgary, Alberta T2N 1N4, Canada
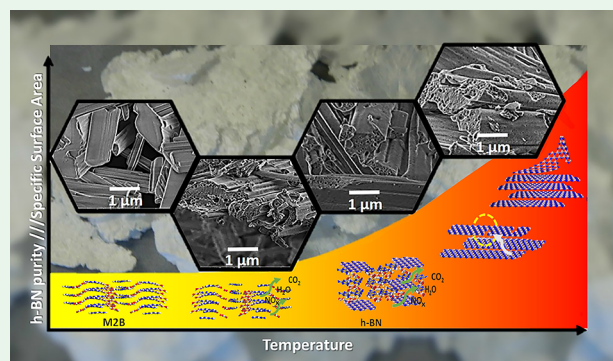
[‡]Division of Engineering in Medicine, Department of Medicine, Brigham and Women's Hospital, Harvard Medical School, Cambridge, Massachusetts 02139, United States

[§]Harvard−MIT Division of Health Sciences and Technology, Massachusetts Institute of Technology, Cambridge, Massachusetts 02139, United States

Ⓢ Supporting Information

ABSTRACT: A well-known ceramic material, hexagonal boron nitride (h-BN), has a number of unique properties, including structural and porosity features, that make it suitable for a wide range of industrial applications. Hierarchical porosity and high specific surface area are desirable properties for adsorption processes such as water and air cleaning, hydrogen storage, and drug delivery. These characteristics could be controlled and optimized by synthesis procedures; however, this process requires an understanding of the factors and mechanisms of nanocrystalline h-BN porosity development and textural properties. In this study, we demonstrate that hierarchical porosity displays evidence of the consecutive h-BN synthesis steps and thermal decomposition of intermediants. In addition, evidence

shows that h-BN nanosheets can be folded as a result of van der Waals force interactions at elevated temperatures, which is corroborated by a computational modeling. The biocompatibility of the prepared h-BN was also evaluated to confirm the nontoxicity of the material. The results of this research could aid in the optimization and scaling up of an environmentally friendly h-BN synthesis process and assist in the development of new methods for the production of h-BN at a commercial level.

KEYWORDS: nanocrystalline boron nitride, biocompatibility, hierarchical porosity, simplified synthesis, folded architecture

INTRODUCTION

Boron nitride, commonly called white graphene, was first synthesized in the laboratory in 1962[1] and was patented 4 years later.[2] It is a versatile ceramic material with unique physical, chemical, and thermal properties that can be used for a number of applications,[3] including electronics,[4] nanomedicine,[5] drug delivery,[6] cancer therapy,[7] hydrogen storage,[8] water treatment,[9] cosmetics,[10] and space technology.[11] Similar to graphene, it is thermally stable at high temperatures,[12] has electrical insulating properties,[13] and is therefore commonly used as a thermal conductor.[14] Although boron nitride was identified over a half century ago, in the last 10 years, remarkable research has changed the understanding of the synthesis, surface properties, and reactivity of this material. While in the past boron nitride was believed to be an inert substance that could only be synthesized in the laboratory, in 2013 a naturally occurring material analogous to cubic boron nitride was found in a geological formation in Tibet[15] and in

2015 a study in France demonstrated boron nitride biodegradation.[16]

The properties of hexagonal boron nitride (h-BN), such as hierarchical porosity,[17] hydrophobicity,[18] electronegative surface charge,[19] biodegradability,[16] and high water dispersibility,[7] are important for biomedical applications including drug delivery,[6] cancer therapies,[20] and genome editing.[21,22] Understanding the mechanism of porosity development will open the pathway for desirable characteristic optimization.

Several methods are used to produce h-BN, including (a) chemical vapor deposition,[23] (b) laser ablation, (c) carbonization of nitrogenous organic compounds,[24] and (d) carbon template usage.[25] The morphology and specific surface area (SSA) of h-BN depends on the synthetic method and
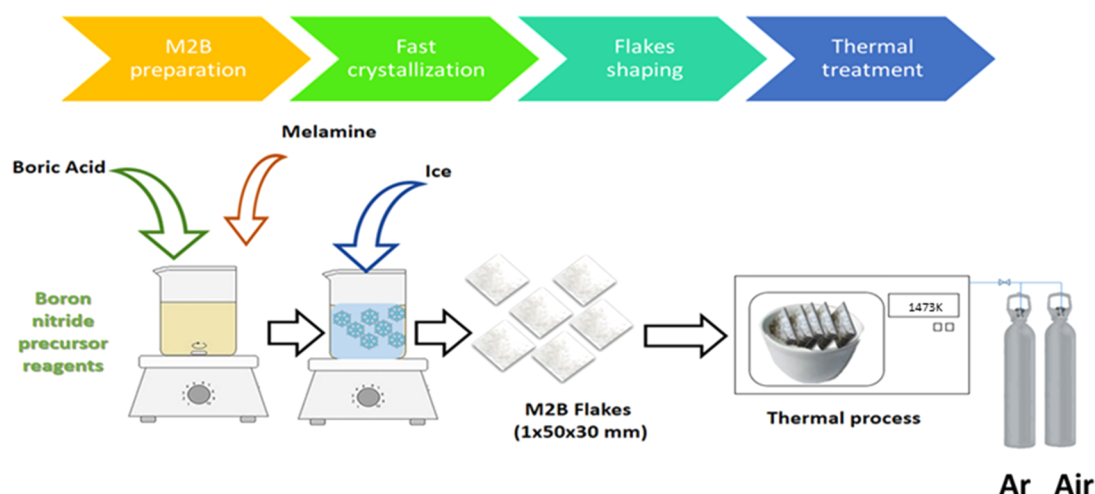
Figure 1. Schematic representation of the experimental setups considered in this study.

experimental conditions employed. A wide variety of different morphological shapes, such as tubes,[26] sheets,[27] rodlike,[28] belts,[29] ribbons,[12] carpetlike,[30] bamboolike,[31] and flowers,[32] have been reported in the literature. In general, all preparation methods of boron nitride require high temperatures and/or pressures. In one of the most feasible methods of synthesis, boric acid and melamine are exposed to high temperatures in an inert atmosphere.[32] This method is one of the safest because, unlike other techniques where ammonia and hydrogen gases are used,[33] this one employs only nonhazardous gases.

This synthetic procedure typically utilizes boric acid and melamine as reactants,[34] relying solely on the reduction of boron by oxidation of an organic material as a source of nitrogen. During these reactions, flue gases such as NO_x and CO_x are generated in an inert atmosphere.[33,34] These reactions have been reported and described earlier by several researchers.[10,33−35] Other research has demonstrated the formation of melamine diborate (M2B), which occurs as a result of hydrogen bonding between melamine and boric acid.[36] Under thermal treatment, the produced crystalline material forms the precursor of h-BN, $(B_4N_3O_2H)$,[37] which is then converted to h-BN under high temperatures under inert atmospheres.

The unique hierarchical porosity and high SSA of h-BN make it a versatile material for adsorption processes[17] that can be utilized in a wide variety of industrial applications.[9,19,38−40] Because understanding the mechanism and factors involved in the h-BN porosity structuring is important for SSA optimization, this study explores and explains. Our approach is to develop a new mechanism for h-BN synthesis and structural optimization using multiple experimental procedures and trials supported by theoretical computational modeling. Herein, we investigated the effects of different variables such as the temperature, porosity, surface area, and precursors' purity. We also evaluated the biocompatibility of h-BN by testing the cytotoxicity on the NIH 3T3 fibroblasts line cells in vitro, a method often used in biocompatibility tests and which has been used previously for evaluating the cytotoxicity of h-BN.[7]

■ MATERIALS AND METHODS

Synthesis of h-BN. Boron nitride was prepared using the O'Connor method[1] with some modifications, where nitrogen and boron are used as the reactants. Boric acid (99% from VWR) was dissolved in boiling water and mixed with melamine (99% from Sigma Aldrich) in a molar ratio of 2:1 for 10 min with continuous magnetic stirring at 350 rpm. After that, the temperature was decreased using an ice bath. Once a solid paste was formed, the mixture was filtered, and the solid product was dried overnight at room temperature and then placed in a reactor vessel that was connected to argon and air cylinders, as presented schematically in Figure 1. Also, the samples were heated from room temperature to 773 K using a Thermolyne model 62700 furnace, with a heating rate of 10 K/min and an air flow rate of 100 cm³/min, and then held for 3 h. At this point, the air was switched to argon, the temperature was raised to 1073 K at a heating rate of 10 K/min and then held for 1 h, and then the temperature was increased to 1473 K and held for another 1 h before cooling to room temperature.

Thermogravimetric Analysis (TGA) and Mass Spectroscopy (MS). To track the reactions during h-BN synthesis, TGA/differential scanning calorimetry (DSC) using a SDT Q600 analyzer (TA Instruments, Inc., New Castle, DE) was carried out to identify the mass losses and the heat flow during the thermal treatment of the synthesis process. The thermogravimetric data were then compared to those of an evolved gas analysis (EGA) that used an online mass spectrometer (Pfeiffer Vacuum GSD 301 O₂, Omnistar, Germany) attached to the TGA/DSC system to detect gas production and to determine the reaction mechanisms that were taking place during the synthesis steps. The inlet to the mass spectrometer from the TGA system was kept heated at around 473 K to avoid condensation of the water vapor produced during the synthesis.

X-ray Diffraction (XRD). XRD characterization was performed to identify the composition of the crystalline phases by their diffraction patterns. Dried powders of prepared h-BN were characterized by XRD using a Rigaku ULTIMA III X-ray diffractometer with Cu Kα radiation as the X-ray source. The scans were performed in the 2θ range of 1−90° using a 0.02° step and a counting time of 1°/min. The crystalline domain sizes were measured using the Scherrer equation,[41] as implemented in the commercial software *JADE* (provided with the diffractometer), by calculating the full width at half-maximum of the peaks fitting the experimental profile to a pseudo-Voigt profile function.[27]

X-ray Photoelectron Spectroscopy (XPS). XPS was carried out with a PHI VersaProbe 5000 spectrometer. The spectra were taken using a monochromatic Al source (1486.6 eV) at 50 W and a beam diameter of 200.0 μm with a takeoff angle of 45°. The samples were pressed onto double-sided tape, and spectra were taken with double neutralization. The binding energies were reported relative to C 1s at 284.8 eV. The sample sputtering protocol involved 10 min of argon sputtering at 45°, 2 kV, 1.5 μA 2 × 2 (10 nm/min). Data were processed using *Multipack* software, applying a Shirley background correction, and fitted with a pseudo-Voigt function.
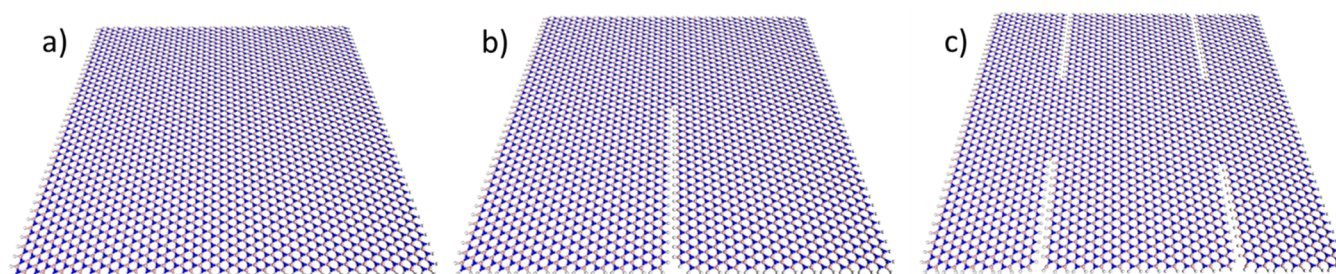
Figure 2. 45° perspective of ball-and-stick representations of (a) an initial 10 nm square sheet model of h-BN, (b) an initial 10 nm square sheet model of h-BN with a lineal atomic fissure, and (c) an initial 10 nm square sheet model of h-BN with four atomic fissures. Blue spheres represent nitrogen atoms, pale orange spheres represent boron atoms, and white spheres represent hydrogen atoms.
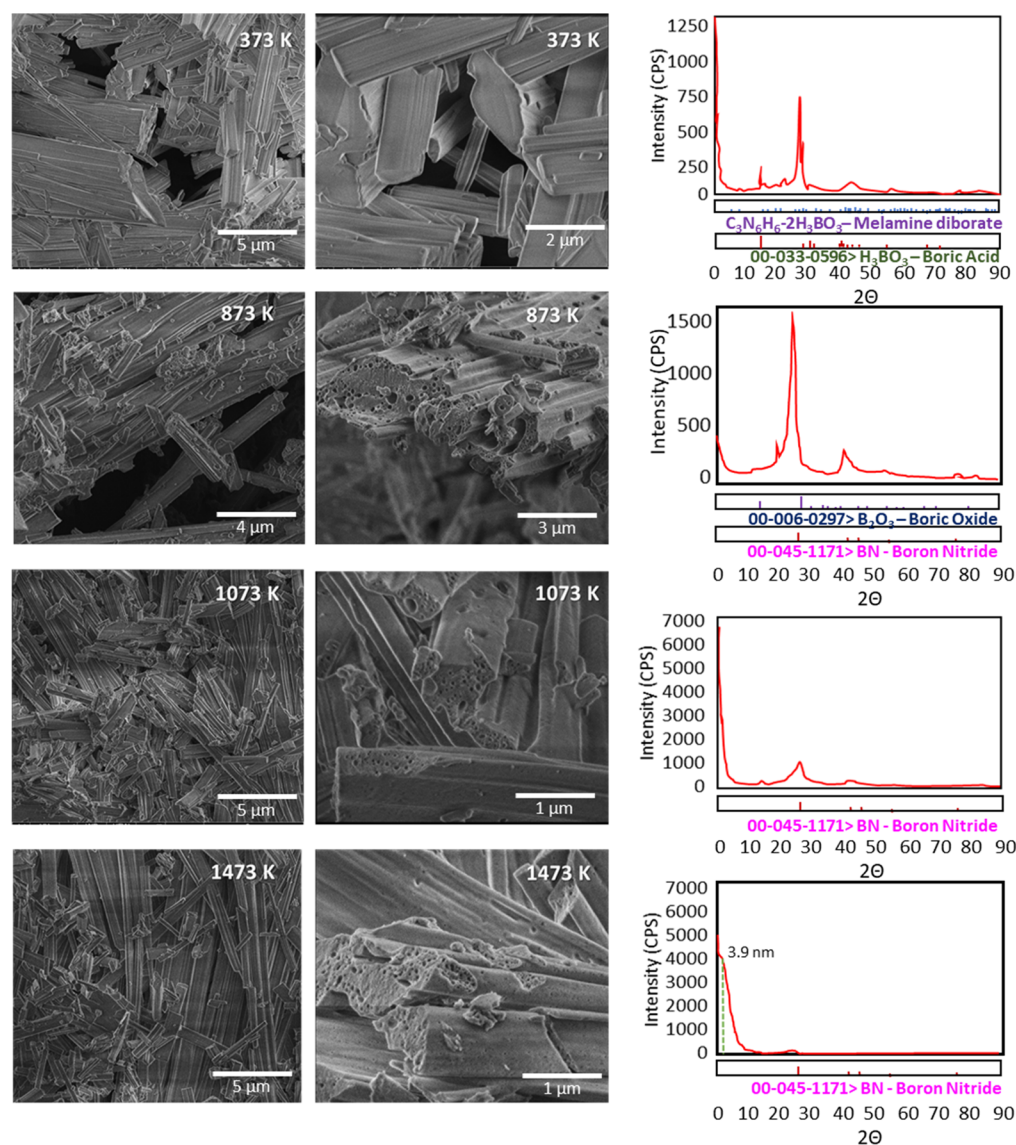
Figure 3. SEM images and X-ray diffractograms for different temperatures during BN synthesis.

Textural Properties. The SSA and pore-size distribution (PSD) of the prepared h-BN were measured following the Brunauer–Emmett–Teller (BET) method. This was achieved by performing nitrogen physisorption at 77 K, using a Tristar 3000 surface area analyzer (Micromeritics Corp., Norcross, GA). The samples were degassed at 423 K under a nitrogen flow overnight prior to analysis. By the same data analysis, the PSD was obtained by processing the obtained adsorption isotherms with the carbon–N_2 2D-NLDFT

heterogeneous surface model present in the *SAIEUS* program for NLDFT models from Micromeritics Corp.

Scanning Electron Microscopy (SEM). SEM was performed to study the surface morphology of the prepared boron nitride. SEM images were taken by a Quanta FEG 250 field-emission microscope made by FEI. The X-ray spectrometry system used was a Bruker Quantax system equipped with a Bruker 5030 silicon drift detector. To view the morphology of the sample, a very small quantity of each

powdered sample was placed over a carbon tape sample holder, which was tapped to release the excess and loose particles before imaging.

High-Resolution Transmission Electron Microscopy (HRTEM). HRTEM images were obtained via a FEI Tecnai F20 FEG transmission electron microscope with an accelerating voltage of 200 kV. This technique was used to corroborate the pore size of the material, matching with the characterization performed with BET and XRD. For analysis, a few milligrams of each sample were dispersed in ethanol, and then a drop of the dispersed solid in the ethanol solution was deposited onto a Formvar carbon–copper grid sample holder.

Computational Modeling. In order to gain some insight into the folding process during the h-BN synthesis, molecular dynamics (MD) simulations were performed using the Forcite module within BIOVIA *Materials Studio 2017* (MS2017) software.[42] The interatomic interactions were described by using the Universal force field[43] to account for the boron and nitrogen in the trigonal geometry, and the charge parameters were assigned according to the charge equilibration method Qeq for MD simulations.[44] The MD simulations were conducted in an *NVT* ensemble at 298 K. The Andersen method[45] was employed in the thermostat to control the thermodynamic temperature with a collision ratio of 1. The time step in the MD simulation was 0.5 fs, and the data were collected every 1 ps. All of the simulations were up to 5 ns as needed to detect several cycles of thermal vibration, and the full-precision trajectory was recorded. The energies and other statistical data (coordinates, velocities, etc.) were stored every 5000 steps during the simulations. An initial 10 nm square sheet of h-BN was built (Figure 2a), and then two different types of fissures were created by deleting some rows of boron and nitrogen atoms from the square, within the sheet, producing two new models as shown in parts b and c in Figure 2, respectively. All of the dangling bonds in the three models were capped with hydrogen atoms.

Cytotoxicity Assessment. To verify whether the produced h-BN has a negative cytotoxic effect on cells, cell viability tests were performed using mouse embryonic 3T3 fibroblast cells.[7,46] Cells were cultivated in Dulbecco's modified Eagle's medium (DMEM)–high glucose. The DMEM–high glucose medium (Gibco, 11965-092) was supplemented with 10 vol % fetal bovine serum (Gibco, 10437-028), 1 vol % L-glutamine (Gibco, 25030-081), and 1 vol % penicillin/streptomycin.

NIH 3T3 fibroblast cell lines were used between passages 2 and 5. Cells were seeded in 96-well plates at a density of 10000 cells/well and left for 24 h to settle. Once cells showed 80% confluence, they were exposed to different concentrations of h-BN. DMEM + h-BN media were prepared by adding h-BN particles, followed by mixing using a sonication bath for 2 h and ultrasonication at 20 kV for 5 min. Ultrasound was employed to enhance the particle dispersion within the media, understanding the hydrophobic behavior of h-BN. Once the particles were well-dispersed, media with different concentrations of h-BN were prepared (0.001–1000 μg/mL). Afterward, cells were incubated with the new media including h-BN particles for 48 h at 37 °C in a humidified atmosphere containing 5 vol % carbon dioxide (CO$_2$).

Presto blue and live/dead assays were performed to determine the cell viability. For PrestoBlue assay, cells were incubated with a commercial reagent; metabolically active cells are expected to reduce the agent and change the absorbance of the solution. After incubation, the absorbance was determined at 570 nm by a microplate reader. The results are expressed as a percentage normalizing the data using cells with no h-BN treatment as a control.

For live and death assays, cells were stained according to the manufacturer's protocol.[47] After staining, cells were observed using a fluorescence optical microscope (Zeiss microscope cell observer) and cells.

■ RESULTS AND DISCUSSION

SEM, XRD, and XPS Characterization. Figure 3 shows SEM images and X-ray diffractograms of samples obtained at different temperatures during thermal treatment. Even though

Table 1. Proposed Reactions during the Synthesis of h-BN

temperature (K)	reaction	equation
403–443	$2H_3BO_3 \rightarrow B_2O_3 + 3H_2O$	(1)
573	$C_3H_6N_6 \rightarrow 3H_2NCN$	(2)
	$R\text{-}NH_2 + O_2 \rightarrow R + NO + H_2O$	(3)
	$NO + {}^1/_2O_2 \rightarrow NO_2$	(4)
773	$HN{=}C{=}NH + H_2O \rightarrow CO(NH_2)_2$	(5)
	$CO(NH_2)_2 + {}^5/_2O_2 \rightarrow CO_2 + 2NO + 2H_2O$	(6)
	$NO + {}^1/_2O_2 \rightarrow NO_2$	(7)
773–1023	$CO(NH_2)_2 + B_2O_3 \rightarrow 2BN + CO_2 + 2H_2O$	(8)
1173	$CO + H_2O \rightarrow CO_2 + H_2$	(9)

lower temperatures were used, compared with other studies,[39,48] synthesized h-BN exhibited a rodlike architecture.[3,29,49] The SEM images did not show notable changes in the external morphology with thermal treatment. However, XRD patterns showed a transition from M2B to h-BN. The average crystalline domain size of the produced h-BN was 15 nm.

In addition, it was possible to determine that the produced material tended to become amorphous because there was a decrease in the intensity of the XRD patterns, as shown in Figure 3, evidencing a change in the crystallinity of the material. M2B showed a well-defined pattern characteristic of its crystalline arrangement at 373 K.[36]

As the temperature increased, the signal intensity decreased as a result of a diminishing of the material crystallinity. It was possible to identify an arrangement of the structural transition for the crystalline phase of M2B[36] transforming to h-BN (Figure 3). That was related to the diminishing of signals detected at 12° and 28°, while the appearance of signals at 22° and 34° in the 2θ axis was reported for a crystalline phase of h-BN.[50]

XPS analysis, as shown in Figure S1, supports the XRD results that demonstrate the appearance of h-BN as boron oxide decreases. Additionally, superficial composition analysis performed by XPS in Figure S1, complemented the characterization of the amorphous components that were not detected by XRD. As the temperature increased, boron oxide disappeared.

The coexistence of h-BN and B$_2$O$_3$ on the surface of the microstructures prepared at 1473 K was identified and replicates the results of a previous study by Zhang et al.[33] Other studies discuss a link between the SSA and oxygen impurities on the surface of h-BN structures.[25,51,52] The presence of functional groups such as C=O in the samples prepared at 873 and 1073 K indicates the formation of urea due to cyanamide oxidation by the thermal decomposition of melamine in the previous reaction step. The interpretation of the obtained results suggests that urea and cyanamide are probable intermediates formed during the h-BN synthesis. Table 1 shows the proposed reaction mechanisms and the intermediates formed during the synthesis process of BN. At 1473 K, the signal corresponding to C=O was not detected, which suggests that complete degradation of urea occurred above 1073 K (see eqs 8 and 9 in Table 1). In addition, XPS analysis demonstrates the conversion of boron on the surface from boric oxide at 873 K to h-BN at 1473 K. The final composition contains 70% of the boron present on the surface as h-BN.
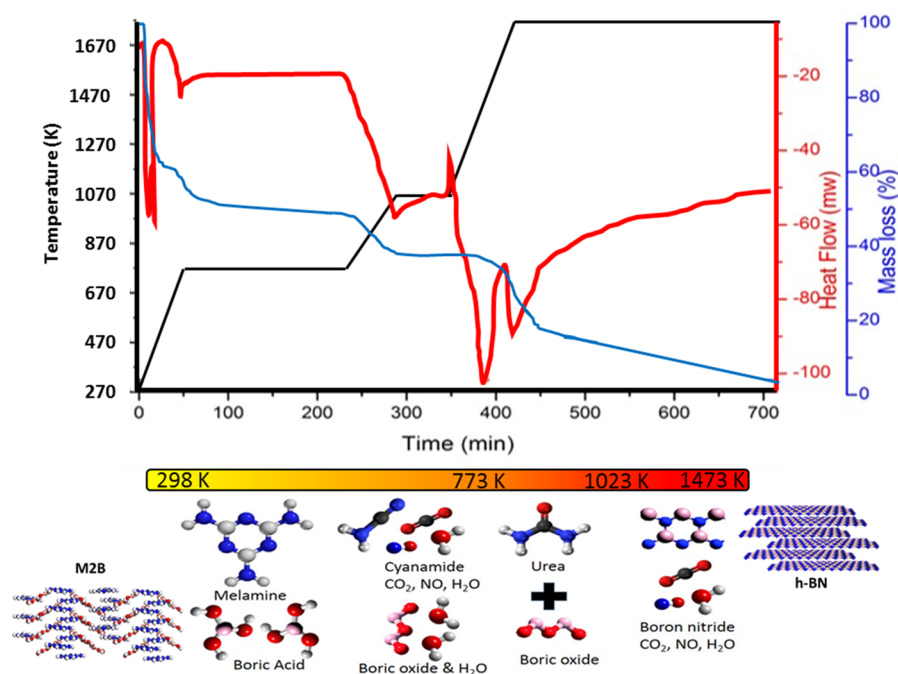
Figure 4. TGA thermograms and schematic representation of the expected reaction pathways during h-BN synthesis.
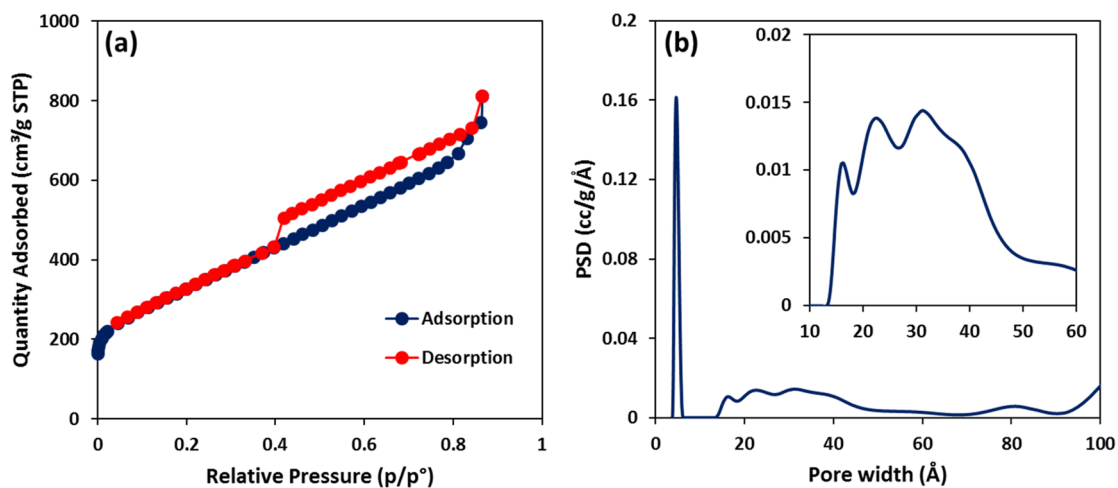

Figure 5. (a) Nitrogen physisorption isotherm plot and (b) PSD curve for the prepared sample of h-BN at 1473 K.
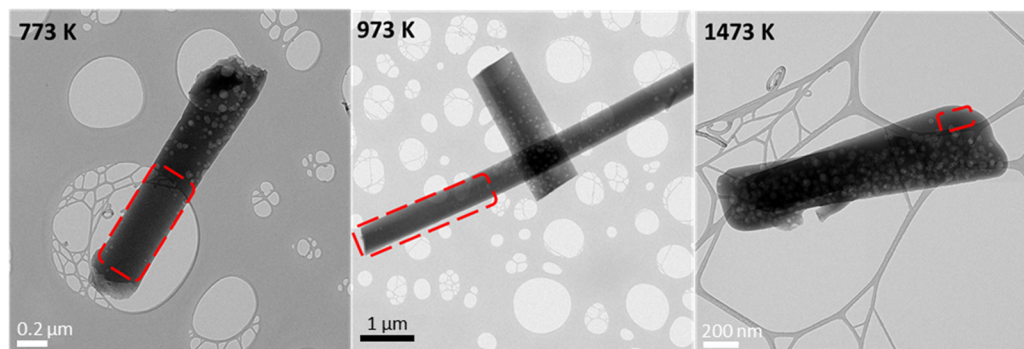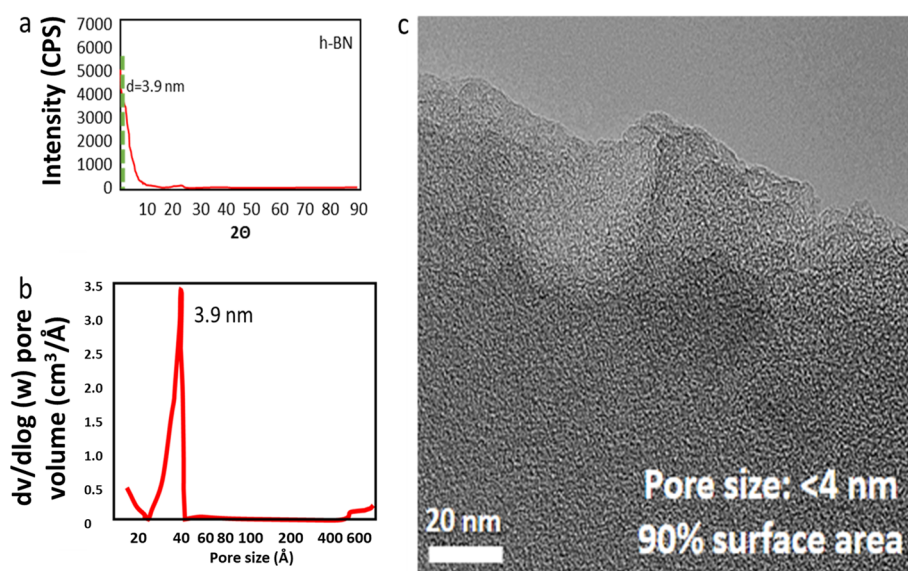

Figure 6. HRTEM images of h-BN produced at different temperatures. The superficial porosity of the material increased progressively regarding the synthesis temperature.

TGA and MS. Experimental data collected by TGA/MS helped to clarify the transition from M2B to h-BN during the thermal conversion pro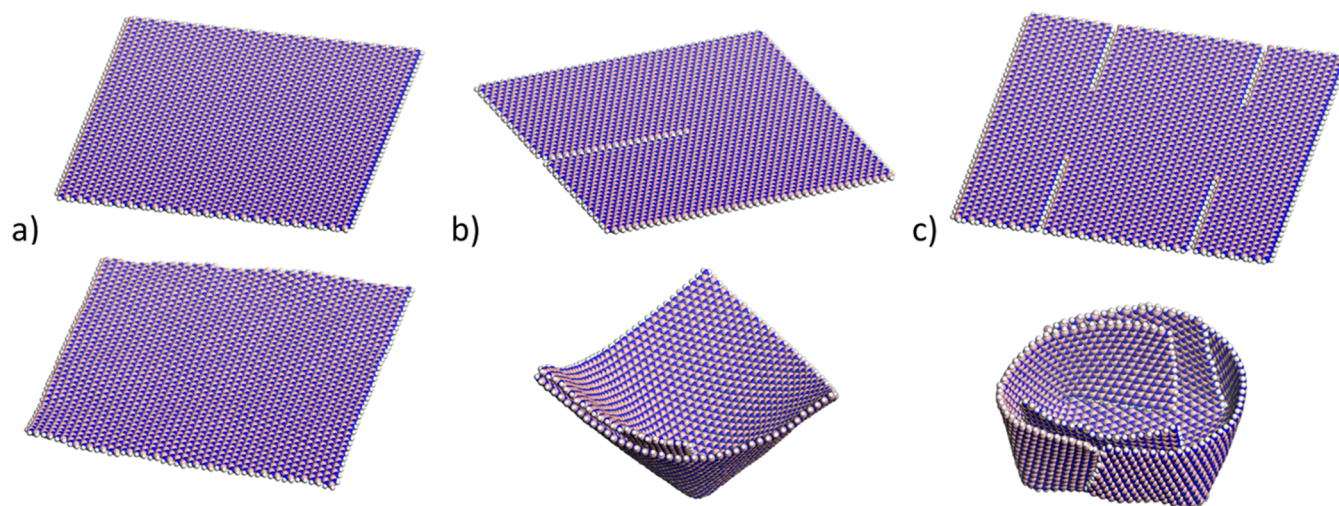cess. Figure 4 displays the TGA data, where the heat flow, mass loss, and temperature ramp are plotted against time. The figure is also supported by Figure S2, which displays the gas analysis performed by MS during the

Figure 7. (a) XRD patterns of h-HB. (b) PSD of the sample. (c) HRTEM image of the material where 4-nm-sized pores are observed.

Table 2. BET SSA and Porosity of h-BN Prepared at Different Temperatures

| T (K)	BET SSA ($m^2\ g^{-1}$)	mesoporosity ($m^2\ g^{-1}$)	microporosity ($m^2\ g^{-1}$)	microporosity area/total SSA	mesopore diameter (nm)	max pore size (nm)
773	336	36	300	0.892	<4	20
973	438	66	372	0.849	<4	40
1073	774	88	686	0.886	<4	60
1473	1162	151	1011	0.870	<4	80

Figure 8. CPK representation of the initial and final configurations of a 10 nm square sheet monolayer of h-BN: (a) without any atomic line cut; (b) with one linear atomic fissure from the center; (c) with four linear atomic fissures. Blue spheres represent nitrogen atoms, pale orange spheres represent boron atoms, and white spheres represent hydrogen atoms.

TGA trial. As seen from the initial mass of reactants, 94 wt % was lost as gas during thermal analysis. The residual material in TGA accounted for 6 wt %, and 70 wt % of it was h-BN. Considering the recovered material as a uniform, the yield recorded was of 4.2% with respect to the initial mass of the reactants.

The mass loss started at the beginning of heating of the material around 373 K. The heat flow recorded an endothermic peak, and MS showed a high-intensity signal corresponding to water (m/e 18 molecular ion). After drying, dehydration of boric acid started at 523 K. An intense peak for

water (m/e 18 molecular ion) was again observed in the MS spectrum. The endothermic peak corresponds to the energy needed for boric acid dehydration.[53] The total mass loss observed by TGA during physical and chemical dehydration of the material was around 15%, and it occurred at 523 K.

Cyanamide was partially oxidized after the dehydration process was promoted by thermal decomposition of melamine. The emitted nitrogen monoxide reacted with oxygen, forming nitrogen dioxide (eqs 3−6 in Table 1). Combustion occurring at 723 K formed CO_2 and nitrogen dioxide. The net heat gained by the system during the production of boron nitride is
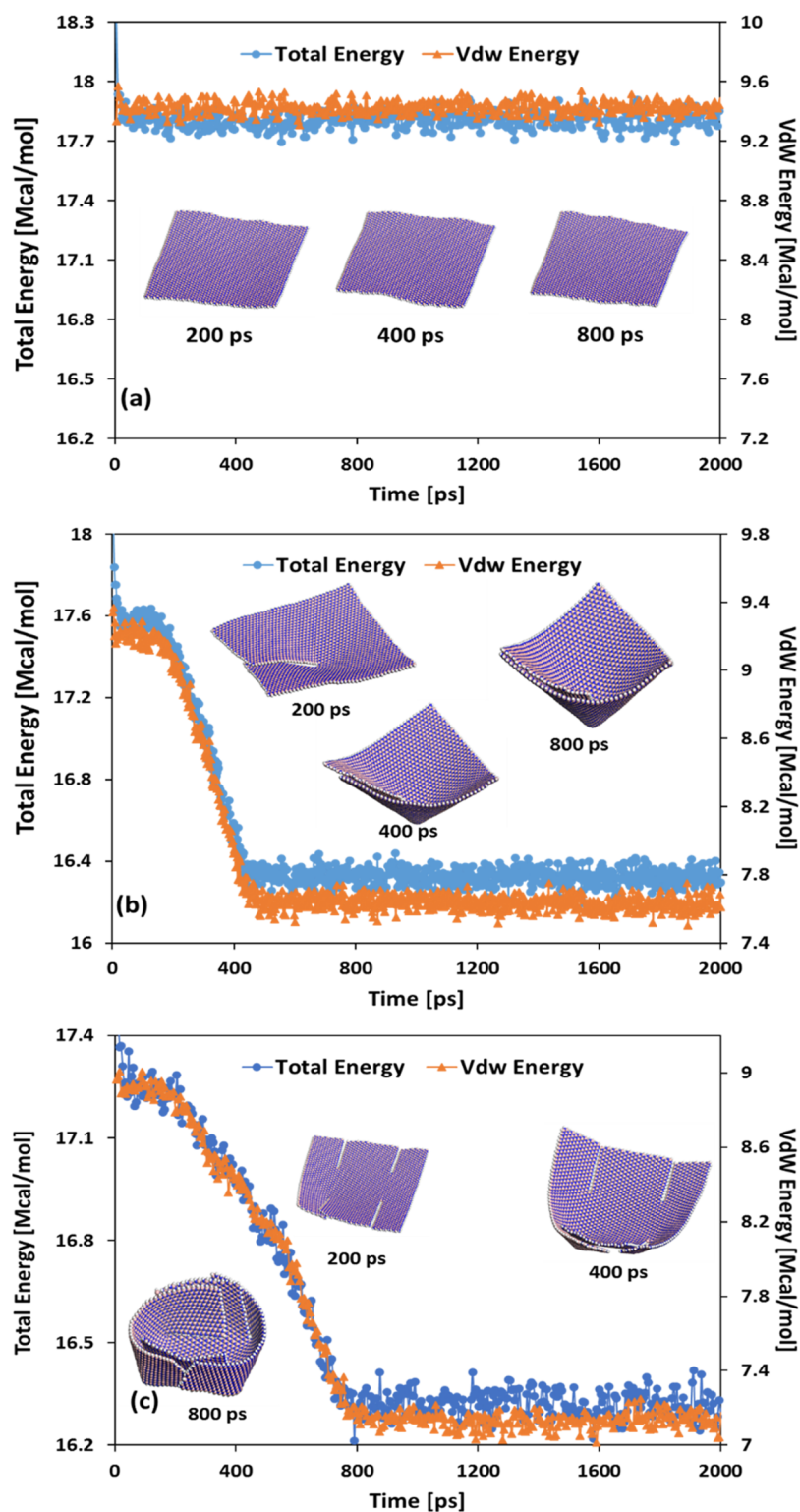
Figure 9. Evolution of the total energy and van der Waals energy as a function of the simulation time: (a) h-BN nanosheet without any atomic line fissure; (b) h-BN nanosheet with one linear atomic fissure from the center; (c) h-BN nanosheet with four linear atomic fissures. The total energy (Mcal/mol) is represented by the blue curve, and the van der Waals energy (Mcal/mol) is represented by the orange curve. Insets show the configurations of the nanosheets at 200, 400, and 800 ps for each model, respectively.

larger than the heat evolved during combustion of the carbon substrate, resulting in the disappearance of the exothermic peak. Figure 4 displays the resulting heat changes around 723 K together with a pictorial representation of the reaction pathways.[34]

After combustion of the organic material, the gas flow switched to argon. After the change to an inert atmosphere, the production of carbon and nitrogen oxides persisted. It is considered that the oxygen required for those oxidation processes came from the remaining boron oxide. The release of
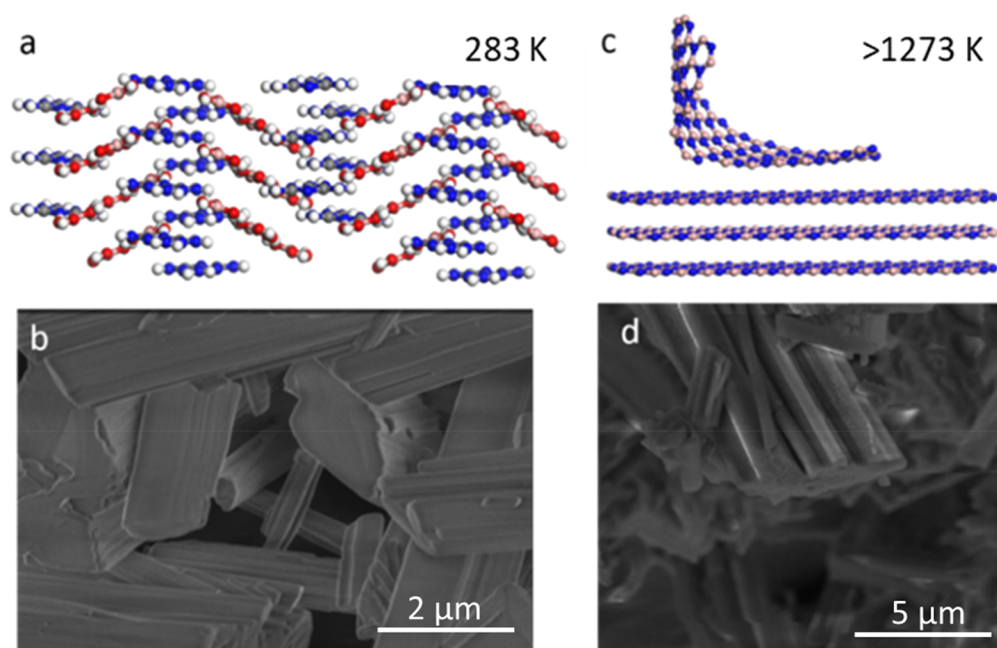
Figure 10. Comparison between the proposed model of M2B and BN SEM images: (a) molecular representation of M2B; (b) SEM image for M2B; (c) h-BN nanosheet representation obtained from computational modeling; (d) SEM image of h-BN showing folded sheets in the upper side of a lamellar arrangement.

oxygen by the reduction of boron promoted the formation of boron nitride.

XPS results show that the amount of boron oxide at the surface of the material was inversely proportional to the temperature.

As an early conclusion, we propose that the release of gases from the surface of the material contributed to the formation of pores.[25] In fact, other studies reported a proportional relationship between the amount of impurities (remaining reactants) and SSA.[25,35,51,52]

Table 1 shows the proposed reaction mechanisms with temperature, based on the experimental data of TGA, EGA, and XPS.

Textural Analysis. Textural analysis showed an ordered hierarchical porosity development process, where the high temperature was the main factor responsible for these changes because the porosity increased progressively along the thermal treatment. This fact can be obviously explained by the obtained adsorption isotherms and PSD for the prepared h-BN at temperatures of 773 K (Figure S4), 973 K (Figure S5), 1073 K (Figure S6), and 1473 K (Figure 5). As shown, the prepared h-BN samples at low temperatures (i.e., 773, 973, and 1073 K) have mainly microporous structure and low mesoporosity. For the prepared sample at high temperature (1473 K), as shown in Figure 5a, the obtained isotherm yields type IV according to IUPAC classifications. As seen, this isotherm, compared with that obtained at lower temperatures, has different shapes because of the porosity variation, forming a new generation for the PSD (Figure 5b). Hence, two porosity-sized regions can be observed: below 2 nm and in the range of 2−4 nm. Below 2 nm, most of the porosity was observed (microporosity). However, there is a significant distribution of pores in the mesoporous range (2−4 nm), as was observed with use of the Barrett−Joyner−Halenda model. Having such a PSD agreed well with the obtained XRD pattern (Figure 7) that shows a low angle peak in a long-range order in

the 3D space. The XRD patterns of h-BN showed a signal at 2θ = 3.5, which is characteristic of mesoporous-ordered materials,[54] indicating a 3.9-nm-ordered 3D arrangement of the nanopores in the obtained material. Figure 6 displays HRTEM images of the material produced at different temperatures, with areas without visible pores indicated in red. Pores on the surface or inside h-BN structures match the HRTEM images (Figure 7), which along with the BET textural analysis verifies that the porosity and SSA increased as the temperature increased (Table 2). Hence, a highly ordered porosity arrangement was detected by matching the BET, HRTEM, and XRD characterizations. In conclusion, increasing the temperature (thermal treatment) progressively increased the porosity. With an increase in the temperature, conversion of the remaining reactants causes an increase in the number of pores until they collapsed, changing the surface morphology (Figures 6 and 7). The ratio of the microporosity and SSA remained the same regardless of the temperature, providing evidence of the uniformity of the hierarchical porosity development.

Computational Modeling for the Scrolling Process. Computational modeling was used to determine the amount of M2B that may occupy that volume before conversion and the number of corresponding atoms for further mass balance analysis (Figure S6), and the results of computational modeling demonstrate the structural changes of h-BN during the thermal treatment after synthesis. Figure 8 shows the initial and final configurations of the 10 nm sheet after MD simulations (see the detailed video 1). Figure 8 shows a nanosheet that must have had some internal atomic line defects, triggering the scrolling process. The preparation method, characteristic of the starting precursor, and the way that it is treated all may influence the production of scrolls. While the melamine diborate precursor has an almost lamellar configuration, the formation of atomic defects during the transformation induces the scrolling process.
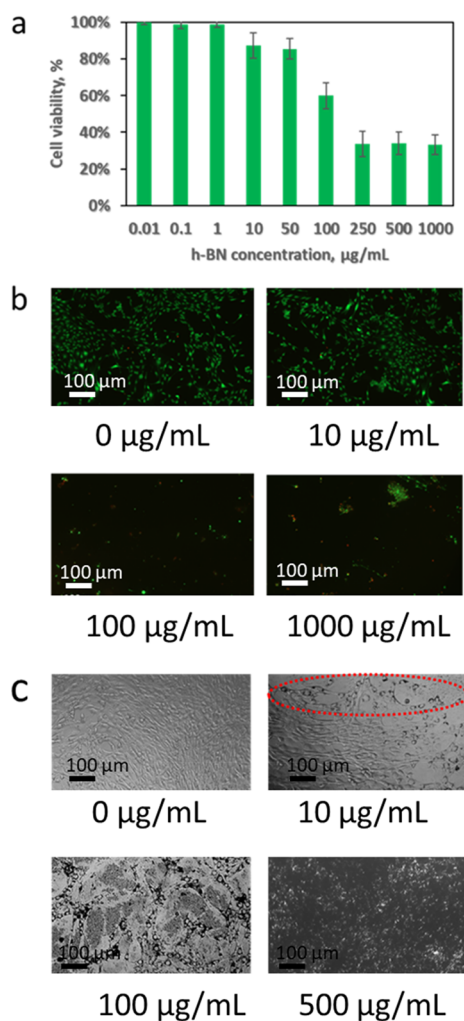
Figure 11. Results of the biocompatibility test: (a) Cell viability evaluated by PrestoBlue assay. The 3T3 cells showed acceptable compatibility at ranges below 50 μg/mL. (b) Live/dead assay results of 3T3 cells exposed to different concentrations of h-BN. (c) Bright-field micrographs of 3T3 cells exposed to h-BN.

As shown in Figure 8b, a simple fissure from the center of the square to the border induces the scrolling of the nanosheet, producing a triangular cone-shaped material, while four linear atomic fissures (Figure 8c) also induce the scrolling but form a basket-shaped configuration.

Figure 9a and video 2 demonstrate that without this atomic line fissure the nanosheet shows surface fluctuations like a "waving flag" without folding or scrolling. In cases where atomic line defects exist, e.g., Figure 9b,c (and videos 2 and 3), the scrolling is spontaneous, the total energy in the system decreases, and the system reaches a more stable state. For the nanosheet with one linear atomic fissure (Figure 8b), the formation of the triangular cone-shaped configuration decreased the total energy by almost 1.3 Mcal/mol, and the equilibrium configuration is obtained after 400 ps. The formation of the basket-shaped configuration from a nanosheet with four linear atomic fissures (Figure 8c) decreases the total energy by almost 1.0 Mcal/mol, but the final equilibrium configuration is obtained beyond 800 ps. In a previous configuration occurring around 400 ps (Figure 9c), a cone-shaped configuration appears to be forming, but the reorganization continues to produce the basket-shaped model.

As shown in Figure 9, the van der Waals energies follow the same trend as the total energies, indicating that these interactions determine the final configuration. Scrolling occurred when the van der Waals energies decreased by almost 1.8 Mcal/mol. From these data, we can conclude that atomic fissure lines are necessary to trigger the folding of the nanosheet of h-BN; van der Waals interactions are the primary force behind the folding of the sheets. Figure 10 shows a comparison between the molecular representations of M2B molecules before reaction and h-BN folded sheets after thermal treatment. The molecular representations were also compared with the SEM images.

Cytotoxicity Assessment. The cellular viability was determined by in vitro testing after incubation of 3T3 fibroblasts with several h-BN concentrations and then analysis via Prestoblue assay. The results showed that h-BN was nontoxic in moderate concentrations of 10 μg/mL, but the cell viability decreased to 85% above 50 μg/mL (Figure 11a). These results are also indicated in Figure 11b, where the cells were analyzed and fluorescently labeled by live and dead assay to demonstrate the biocompatibility of the material. Dead cells are labeled in red and live cells in green, showing the compatibility of the material at concentrations below 50 μg/mL.

Bright-field micrographs are presented in Figure 11c; normal cellular morphology under exposure of h-BN can be observed at low h-BN concentrations. However, above 100 μg/mL, sedimentation of h-BNs can be observed in the micrograph, where dark aggregates are covering the cell surface. This observation is expected because of the hydrophobic nature of the material, where a similar phenomenon was reported by another research group.[55]

It is expected that, because of the size, the material will be internalized and at high concentrations cause cytotoxic effects such as the production of reactive oxygen species and cytokines, disruption of the cellular signaling pathway, cell cycle dysregulation, DNA damage, and apoptosis.[56]

Internalization of the particles can be visibly identified in the bright-field micrographs, where dark areas are surrounding the perinuclear region of the cells.

The results suggest that h-BN uptake, material morphology, and hydrophobicity may be correlated with the biocompatibility. A previous study using the same cell line concluded that the toxicity of h-BN is strongly correlated with the intracellular particle accumulation and morphological straightness.[55,57] A smoother border morphology (as observed in Figures 6 and 10) and more rapid aggregation of particles could improve the biocompatibility, preventing exposure of the cells to individual h-BN particles.[57]

When the h-BN dosage was above 250 μg/mL, particle aggregation and sedimentation were observed, and as a result, the cell membranes were completely covered by a h-BN layer, affecting the biocompatibility of the microparticle system by increasing the cell membrane—material interactions and particle uptake.

To increase its biocompatibility and enhance its water dispersion, this material could be coated with polymers such as poly(ethylene glycol) or surfactants such as poly(vinyl alcohol) in future studies.[58−60] The biocompatibility test of h-BN demonstrates a positive safety tolerance if the material is applied at moderate concentrations; however, it points the necessity of increasing its hydrophilicity to decrease its

sedimentation and increased interaction at the level of the cellular membrane.

CONCLUSIONS

In this work, we have shown that the characteristic structure and hierarchical porosity exhibited by h-BN correspond to footprints left during the synthesis process. The prepared h-BN showed a porosity promoted mainly by gas released during conversion of the precursors by a multiple crystalline nucleation process. Nanocrystalline domains of h-BN grow up over the existing microstructures of M2B and the core becomes porous. The computational modeling and SEM and HRTEM images concluded that the high temperature is responsible for folding of the h-BN structures, while the presence of defects in the upper layers and van der Waals interactions also promoted the folding process. The non-toxicity of the material was demonstrated at moderate concentrations, evaluating live/dead tests on 3T3 line cells and cytotoxicity by Prestoblue, which makes the produced material safe for environmental applications.

ASSOCIATED CONTENT

Ⓢ Supporting Information

The Supporting Information is available free of charge on the ACS Publications website at DOI: 10.1021/acsanm.8b00765.

> XPS characterization, MS spectra of gases during BN synthesis, and nitrogen physisorption isotherms with the corresponding PSDs at low temperatures (PDF)
> Supporting animation video for the BN folding process (MP4)
> Supporting animation video for the BN folding process (MP4)
> Supporting animation video for the BN folding process (MP4)

AUTHOR INFORMATION

Corresponding Author

*E-mail: nassar@ucalgary.ca.

ORCID

Gerardo Vitale: 0000-0002-3142-0898
Azfar Hassan: 0000-0003-0175-2549
Nashaat N. Nassar: 0000-0001-9014-542X

Notes

The authors declare no competing financial interest.

ACKNOWLEDGMENTS

REFERENCES

(1) O'Connor, T. E. Synthesis of Boron Nitride. *J. Am. Chem. Soc.* **1962**, *84*, 1753−1754.

(2) Lenihan, W. S., Park, F., Reidl, R. W. Method for Preparing Boron Nitride. U.S. Patent 3,241,918, March 22, 1966

(3) Lin, J.; Xu, L.; Huang, Y.; Li, J.; Wang, W.; Feng, C.; Liu, Z.; Xu, X.; Zou, J.; Tang, C. Ultrafine Porous Boron Nitride Nanofibers Snthesized via a Freeze Drying and Pyrolysis Process and Their Adsorption Properties. *RSC Adv.* **2016**, *6* (2), 1253−1259.

(4) Xiong, M.; Fan, C.; Zhao, Z.; Wang, Q.; He, J.; Yu, D.; Liu, Z.; Xu, B.; Tian, Y. Novel Three-Dimensional Boron Nitride Allotropes from Compressed Nanotube Bundles. *J. Mater. Chem. C* **2014**, *2* (34), 7022−7028.

(5) Chen, Y. *Nanotubes and Nanosheets: Functionalization and Applications of Boron Nitride and Other Nanomaterials*; CRC Press, 2015.

(6) Roosta, S.; Nikkhah, S. J.; Sabzali, M.; Hashemianzadeh, S. M. Molecular Dynamics Simulation Study of Boron Nitride Nanotubes as a Drug Carrier: from Encapsulation to Releasing. *RSC Adv.* **2016**, *6* (11), 9344−9351.

(7) Weng, Q.; Wang, B.; Wang, X.; Hanagata, N.; Li, X.; Liu, D.; Wang, X.; Jiang, X.; Bando, Y.; Golberg, D. Highly Water-Soluble, Porous, and Biocompatible Boron Nitrides for Anticancer Drug Delivery. *ACS Nano* **2014**, *8* (6), 6123−6130.

(8) Lei, W.; Zhang, H.; Wu, Y.; Zhang, B.; Liu, D.; Qin, S.; Liu, Z.; Liu, L.; Ma, Y.; Chen, Y. Oxygen-doped Boron Nitride Nanosheets with Excellent Performance in Hydrogen Storage. *Nano Energy* **2014**, *6*, 219−224.

(9) Li, J.; Lin, J.; Xu, X.; Zhang, X.; Xue, Y.; Mi, J.; Mo, Z.; Fan, Y.; Hu, L.; Yang, X.; Zhang, J.; Meng, F.; Yuan, S.; Tang, C. Porous Boron Nitride with a High Surface Area: Hydrogen Storage and Water Treatment. *Nanotechnology* **2013**, *24* (15), 155603.

(10) Ansaloni, L. l. M. r. S.; de Sousa, E. M. B. Boron Nitride Nanostructured: Synthesis, Characterization and Potential Use in Cosmetics. *Mater. Sci. Appl.* **2013**, *4* (7), 22.

(11) Lin, Y.; Williams, T. V.; Cao, W.; Elsayed-Ali, H. E.; Connell, J. W. Defect Functionalization of Hexagonal Boron Nitride Nanosheets. *J. Phys. Chem. C* **2010**, *114* (41), 17434−17439.

(12) Lin, Y.; Connell, J. W. Advances in 2D Boron Nitride Nanostructures: Nanosheets, Nanoribbons, Nanomeshes, and Hybrids with Graphene. *Nanoscale* **2012**, *4* (22), 6908−6939.

(13) Han, W.-Q., Anisotropic Hexagonal Boron Nitride Nanomaterials: Synthesis and Applications. *Nanotechnologies for the Life Sciences*; Wiley-VCH Verlag GmbH & Co. KGaA, 2007.

(14) Haubner, R.; Wilhelm, M.; Weissenbacher, R.; Lux, B. Boron Nitrides—Properties, Synthesis and Applications. *Structure Bonding (Berlin)*; Springer-Verlag: Berlin, 2002; Vol. 102, pp 4−38.

(15) Dobrzhinetskaya, L. F.; Wirth, R.; Yang, J.; Green, H. W.; Hutcheon, I. D.; Weber, P. K.; Grew, E. S. Qingsongite, Natural Cubic Boron Nitride: The First Boron Mineral from the Earth's Mantle. *Am. Mineral.* **2014**, *99* (4), 764−772.

(16) Kurapati, R.; Backes, C.; Ménard-Moyon, C.; Coleman, J. N.; Bianco, A. White Graphene Undergoes Peroxidase Degradation. *Angew. Chem., Int. Ed.* **2016**, *55* (18), 5506−5511.

(17) Bernard, S.; Miele, P. Nanostructured and Architectured Boron Nitride from Boron, Nitrogen and Hydrogen-containing Molecular and Polymeric Precursors. *Mater. Today* **2014**, *17* (9), 443−450.

(18) Pham, T.; Goldstein, A. P.; Lewicki, J. P.; Kucheyev, S. O.; Wang, C.; Russell, T. P.; Worsley, M. A.; Woo, L.; Mickelson, W.; Zettl, A. Nanoscale Structure and Uperhydrophobicity of Sp2-bonded Boron Nitride Aerogels. *Nanoscale* **2015**, *7* (23), 10449−10458.

(19) Chen, X.; Jia, S.; Ding, N.; Shi, J.; Wang, Z. Capture of Aromatic Organic Pollutants by Hexagonal Boron Nitride Nanosheets: Density Functional Theoretical and Molecular Dynamic Investigation. *Environ. Sci.: Nano* **2016**, *3* (6), 1493−1503.

(20) Li, X.; Wang, X.; Zhang, J.; Hanagata, N.; Wang, X.; Weng, Q.; Ito, A.; Bando, Y.; Golberg, D. Hollow Boron Nitride Nanospheres as Boron Reservoir for Prostate Cancer Treatment. *Nat. Commun.* **2017**, *8*, 13936.

(21) Ferreira, T. H.; Hollanda, L. M.; Lancellotti, M.; de Sousa, E. M. B. BoronNitrideNanotubes Chemically Functionalized with Glycol Chitosan forGene Transfection in Eukaryotic Cell Lines. *J. Biomed. Mater. Res., Part A* **2015**, *103* (6), 2176–2185.

(22) Şen, Ö.; Çobandede, Z.; Emanet, M.; Bayrak, Ö. F.; Çulha, M. Boron Nitride Nanotubes for Gene Silencing. *Biochim. Biophys. Acta, Gen. Subj.* **2017**, *1861* (9), 2391–2397.

(23) Ma, R.; Bando, Y.; Sato, T. CVD synthesis of boron nitride nanotubes without metal catalysts. *Chem. Phys. Lett.* **2001**, *337*, 61.

(24) Çamurlu, H. E.; Sevinç, N.; Topkaya, Y. Role of boron carbide in carbothermic formation of Hexagonal Boron Nitride. *J. Mater. Sci.* **2006**, *41* (15), 4921–4927.

(25) Dibandjo, P.; Bois, L.; Chassagneux, F.; Miele, P. Thermal Stability of Mesoporous Boron NitrideTemplated with a Cationic Surfactant. *J. Eur. Ceram. Soc.* **2007**, *27* (1), 313–317.

(26) Xu, X. G.; Gilburd, L.; Bando, Y.; Golberg, D.; Walker, G. C. Defects and Deformation of Boron Nitride Nanotubes Studied by Joint Nanoscale Mechanical and Infrared Near-Field Microscopy. *J. Phys. Chem. C* **2016**, *120* (3), 1945–1951.

(27) Wang, X.; Zhi, C.; Weng, Q.; Bando, Y.; Golberg, D. Boron Nitride Nanosheets: Novel Syntheses and Applications in Polymeric Composites. *J. Phys.: Conf. Ser.* **2013**, *471* (1), 012003.

(28) Gao, L.; Li, J. Preparation of Nanostructured Hexagonal Boron Nitride Powder. *J. Am. Ceram. Soc.* **2003**, *86* (11), 1982–1984.

(29) Weng, Q.; Wang, X.; Zhi, C.; Bando, Y.; Golberg, D. Boron Nitride Porous Microbelts for Hydrogen Storage. *ACS Nano* **2013**, *7* (2), 1558–1565.

(30) Zhang, X.; Lian, G.; Zhang, S.; Cui, D.; Wang, Q. Boron Nitride Nanocarpets:Controllable Synthesis and Their Adsorption Performance to Organic Pollutants. *CrystEngComm* **2012**, *14* (14), 4670–4676.

(31) Bourgeois, L.; Bando, Y.; Sato, T. Tubes of Rhombohedral Boron Nitride. *J. Phys. D: Appl. Phys.* **2000**, *33* (15), 1902.

(32) Wang, P.; Li, H.; Gao, Q.; Li, P.-Z.; Yao, X.; Bai, L.; Nguyen, K. T.; Zou, R.-Q.; Zhao, Y. Fabrication of Novel Hybrid Nanoflowers from Boron Nitride Nanosheets and Metal-organic Frameworks: a Solid Acid Catalyst with Enhanced Catalytic Performance. *J. Mater. Chem. A* **2014**, *2* (44), 18731–18735.

(33) Zhang, L.; Gu, Y.; Ge, C.; Chang, J. A Facile Continuous Production of Hexagonal Boron Nitride Powders. *Chem. Lett.* **2011**, *40* (10), 1127–1128.

(34) Hagio, T.; Kobayashi, K.; Sato, T. Formation of Hexagonal BN by Thermal Decomposition of Melamine Diborate. *Nippon Seramikkusu Kyokai Gakujutsu Ronbunshi* **1994**, *102* (1191), 1051–1054.

(35) Brožek, V.; Hubáček, M. A contribution to the crystallochemistry of boron nitride. *J. Solid State Chem.* **1992**, *100* (1), 120–129.

(36) Kawasaki, T.; Kuroda, Y.; Nishikawa, H. The Crystal Structure of Melamine Diborate. *Nippon Seramikkusu Kyokai Gakujutsu Ronbunshi* **1996**, *104*, 935.

(37) Ma, R.; Bando, Y.; Sato, T.; Kurashima, K. Growth, Morphology, and Structure of Boron Nitride Nanotubes. *Chem. Mater.* **2001**, *13* (9), 2965–2971.

(38) Li, J.; Huang, Y.; Liu, Z.; Zhang, J.; Liu, X.; Luo, H.; Ma, Y.; Xu, X.; Lu, Y.; Lin, J.; Zou, J.; Tang, C. Chemical Activation of Boron NitrideFibers for Improved Cationic Dye Removal Performance. *J. Mater. Chem. A* **2015**, *3* (15), 8185–8193.

(39) Li, J.; Xiao, X.; Xu, X.; Lin, J.; Huang, Y.; Xue, Y.; Jin, P.; Zou, J.; Tang, C. Activated Boron Nitride as an Effective Adsorbent for Metal Ions and Organic Pollutants. *Sci. Rep.* **2013**, *3*, 3208.

(40) Lei, W.; Portehault, D.; Liu, D.; Qin, S.; Chen, Y. Porous boron nitride nanosheets for effective water cleaning. *Nat. Commun.* **2013**, *4*, 1777.

(41) Scherrer, P. G. N. Bestimmung der Grosse und der Inneren Struktur von Kolloidteilchen Mittels Rontgenstrahlen, Nachrichten von der Gesellschaft der Wissenschaften. *Math. Phys.* **1918**, *2*, 98–100.

(42) *BIOVIA: Materials Studio Modeling and Simulation Software 2017*; Dassault Systemes, 2016.

(43) Rappe, A. K.; Casewit, C. J.; Colwell, K. S.; Goddard, W. A.; Skiff, W. M. UFF, A Full Periodic Table Force Field for Molecular Mechanics and Molecular Dynamics Simulations. *J. Am. Chem. Soc.* **1992**, *114* (25), 10024–10035.

(44) Rappe, A. K.; Goddard, W. A. Charge Equilibration for Molecular Dynamics Simulations. *J. Phys. Chem.* **1991**, *95* (8), 3358–3363.

(45) Andersen, H. C. Molecular Dynamics Simulations at Constant Pressure and/or Temperature. *J. Chem. Phys.* **1980**, *72* (4), 2384–2393.

(46) Ciofani, G.; Danti, S.; Genchi, G. G.; Mazzolai, B.; Mattoli, V. Boron Nitride Nanotubes: Biocompatibility and Potential Spill-Over in Nanomedicine. *Small* **2013**, *9* (9–10), 1672–1685.

(47) Riss, T. R.; Moravec, R. A.; Niles, A.; Benink, H.; Worzella, T.; Minor, L.; Storts, D.; Reid, Y. *Cell Viability Assays in Assay Guidance Manual.* **2016**, 1–31.

(48) Gautam, C.; Tiwary, C. S.; Jose, S.; Brunetto, G.; Ozden, S.; Vinod, S.; Raghavan, P.; Biradar, S.; Galvao, D. S.; Ajayan, P. M. Synthesis of Low-Density, Carbon-Doped, Porous Hexagonal Boron Nitride Solids. *ACS Nano* **2015**, *9* (12), 12088–12095.

(49) Zhang, L.; Zhang, G.; Chen, C.; Li, L.; Xia, T.; Shi, K. A Facile Route to Synthesise h-BN-FeB49 Nanocomposites with Magnetic and FluorescentProperties. *CrystEngComm* **2011**, *13* (23), 7153–7160.

(50) Pease, R. S. An X-ray study of boron nitride. *Acta Crystallogr.* **1952**, *5* (3), 356–361.

(51) Hagio, T.; Nonaka, K.; Sato, T. Microstructural Development withCrystallization of Hexagonal Boron Nitride. *J. Mater. Sci. Lett.* **1997**, *16* (10), 795–798.

(52) Hagio, T.; Kobayashi, K.; Yoshida, H.; Yasunaga, H.; Nishikawa, H. Sintering of the Mechanochemically Activated Powders of Hexagonal Boron Nitride. *J. Am. Ceram. Soc.* **1989**, *72* (8), 1482–1484.

(53) Sevim, F.; Demir, F.; Bilen, M.; Okur, H. Kinetic Analysis of Thermal Decomposition of Boric Acid from Thermogravimetric Data. *Korean J. Chem. Eng.* **2006**, *23* (5), 736–740.

(54) Choi, M.; Cho, H. S.; Srivastava, R.; Venkatesan, C.; Choi, D.-H.; Ryoo, R. Amphiphilic Organosilane-directed Synthesis of Crystalline Zeolite with Tunable Mesoporosity. *Nat. Mater.* **2006**, *5* (9), 718–723.

(55) Rasel, M. A. I.; Li, T.; Nguyen, T. D.; Singh, S.; Zhou, Y.; Xiao, Y.; Gu, Y. Biophysical Response of Living Cells to Boron Nitride Nanoparticles: Uptake Mechanism and Bio-mechanical Characterization. *J. Nanopart. Res.* **2015**, *17* (11), 441.

(56) Adabi, M.; Naghibzadeh, M.; Adabi, M.; Zarrinfard, M. A.; Esnaashari, S. S.; Seifalian, A. M.; Faridi-Majidi, R.; Tanimowo Aiyelabegan, H.; Ghanbari, H. Biocompatibility and Nanostructured Materials: Applications in Nanomedicine. *Artif. Cells, Nanomed., Biotechnol.* **2017**, *45* (4), 833–842.

(57) Horváth, L.; Magrez, A.; Golberg, D.; Zhi, C.; Bando, Y.; Smajda, R.; Horváth, E.; Forró, L.; Schwaller, B. Vitro Investigation of the Cellular Toxicity of Boron Nitride Nanotubes. *ACS Nano* **2011**, *5* (5), 3800–3810.

(58) Ciofani, G.; Genchi, G. G.; Liakos, I.; Athanassiou, A.; Dinucci, D.; Chiellini, F.; Mattoli, V. A Simple Approach to Covalent Functionalization of Boron Nitride Nanotubes. *J. Colloid Interface Sci.* **2012**, *374* (1), 308–314.

(59) Bhandari, S.; Tiwari, B.; Yapici, N.; Zhang, D.; Yap, Y. K. Introduction to Boron Nitride Nanotubes: Synthesis, properties, Functionalization, and Cutting A2 - Ciofani, Gianni. In *Boron Nitride Nanotubes in Nanomedicine*; Mattoli, V., Ed.; William Andrew Publishing: Boston, 2016; Chapter 1, pp 1–15.

(60) Zhang, H.; Feng, S.; Yan, T.; Huang, D.; Zhi, C.; Nakanishi, H.; Gao, X.-D. Folate-conjugated Boron Nitride Nanospheres for Targeted Delivery of Anticancer Drugs. *Int. J. Nanomed.* **2016**, *11*, 4573–4582.